Accurate measurement of strain at interfaces in 4D-STEM: a comparison of various methods

Christoph Mahr[a,c,*], Knut Müller-Caspary[b], Tim Grieb[a,c], Florian F. Krause[a,c], Marco Schowalter[a,c], Andreas Rosenauer[a,c]

[a] *Institute of Solid State Physics, University of Bremen, Otto-Hahn-Allee 1, D-28359 Bremen, Germany*
[b] *Ernst Ruska-Centre for Microscopy and Spectroscopy with Electrons, Wilhelm-Johnen-Strasse, D-52428 Jülich, Germany*
[c] *MAPEX Center for Materials and Processes, University of Bremen, Bibliothekstr. 1, D-28359 Bremen, Germany*

Abstract

Strain analysis by nano-beam electron diffraction allows for measurements of strain with nanometre resolution in a large field of view. This is done by evaluating distances between diffraction discs in diffraction patterns acquired while a focussed electron beam is scanned across the sample in a transmission electron microscope. The bottleneck of this method is a precise determination of diffraction disc positions, which suffers from the inner structure of the discs caused by dynamical diffraction. Electron beam precession is a tool that solves this problem but it is not commonly available in every microscope. Without precession significant progress has been reported recently by using patterned condenser apertures. The pattern of the aperture is reproduced in patterns of the diffraction discs allowing for a more precise position determination. In this report the accuracy of measured strain profiles using patterned apertures is investigated by evaluation of realistic simulations. This is done especially at interfaces between regions with different lattice plane spacing. It is found by evaluation of the simulations that measured strain profiles are more blurred and hence the accuracy at the interface is worse the more patterns are imprinted to the condenser aperture. An explanation of this effect is given and as a proof of principle a solution to this problem is provided applying geometric phase analysis ptychography.

Keywords: strain measurement, ptychography, interface, 4D-STEM, patterned apertures

1. Introduction

The strain state of a solid strongly influences its functional behaviour. This influence may be intended or not. For example, strain can be used to tune the mobility of charge carriers and hence the performance of electronic devices [1]. Furthermore, adsorption of atoms or molecules on surfaces of solids can cause reversible macroscopic length changes originating from changes of crystal lattice strain, which makes the material an interesting candidate for sensing applications [2]. On the other hand, strain limits the amount of a foreign material that can be incorporated in a host material without the formation of misfit dislocations [3]. For this reason, measurement of strain is important in order to analyse and improve the behaviour of functional materials.

Measurement of strain in a transmission electron microscope (TEM) provides the required spatial resolution in the nanometre or even sub-nanometre region [4, 5, 6, 7, 8]. Strain analysis by nano-beam electron diffraction (NBED) in a TEM has been used to measure strain, because it overcomes some of the major limitations of other TEM-based methods [6, 7, 9, 10]. NBED strain analysis is carried out in the scanning mode (STEM) of the TEM by recording so-called 4D-STEM data sets. In 4D-STEM, the focussed electron beam is scanned across the sample and a diffraction pattern is recorded at each position of the beam. In this manner, the two-dimensional real space of the sample is scanned and at each position a two-dimensional section of the reciprocal space is recorded, giving 4D-STEM methods their name. A review of 4D-STEM results including measurements of strain is given in Ref. [11].

For measurements of strain using NBED the convergence angle of the electron beam is chosen in a way that the diffraction discs in the diffraction pattern do not overlap. Although this is convergent beam electron diffraction (CBED), strain measurement by CBED is usually considered as the method in which strain is measured from the positions of higher-order Laue zone (HOLZ) lines [5]. In contrast, measuring strain by NBED, distances between diffraction discs are evaluated [6, 12, 7, 13]. They depend on the local lattice plane spacing in the region illuminated by the focussed electron beam according to Bragg's law [14]. Strain is obtained from a measurement of distances between diffraction discs and comparison to distances measured in diffraction patterns acquired in a reference region of the sample.

*Corresponding author
Email address: mahr@ifp.uni-bremen.de (Christoph Mahr)

The main advantage of strain analysis by NBED is a large field of view, with a spatial resolution limited by the electron beam diameter [6, 7, 8] given a sufficient sampling of the scan raster. Accurate and precise measurement of strain requires an accurate and precise measurement of distances between diffraction discs and hence an accurate and precise determination of their positions. Disc position detection suffers from the inner structure of the diffraction discs, which originates from dynamical diffraction. This causes additional edges hindering edge detection based position detection techniques [7, 15] or it causes position determination errors in case correlation based techniques are applied while parts of the diffraction discs are dark [7, 9]. This results in precisions of about $\sigma \geq 0.08\,\%$ and accuracies of about $\Delta \geq 0.1\,\%$ [7, 9]. A solution to this problem is electron beam precession [16]. Tilting the electron beam by a small angle α with respect to the optical axis and varying the direction of the tilt azimuthally from 0° to 360° leads to more homogeneous intensity distributions within the diffraction discs, if the camera frame time is chosen long enough to integrate the intensity during a full 360°-cycle of azimuthal tilting. It has been shown experimentally [13, 17, 10] as well as theoretically [9] that this more homogeneous intensity distribution within the diffraction discs improves precision σ and accuracy Δ of measurements of strain strongly, reaching values of $\sigma = 0.02\,\%$ and $\Delta = 0.02\,\%$ [13, 9], respectively.

Details of this method have been investigated theoretically [9, 18], experimentally [19, 20, 21, 22, 8] and with respect to hardware [23, 24, 25, 26, 27]. Many applications characterizing various samples have been published, for example see Refs. [6, 13, 17, 10, 28].

Many groups have tried to improve the precision of the method using condenser apertures with a special pattern [29, 9, 21, 22]. Recently, Zeltmann et al. took up this idea and reported on significantly improved precision using patterned condenser apertures providing also a theoretical reason for this improvement [8]. But they tested this idea only on unstrained samples and hence without interfaces between regions with different lattice plane spacing. However, from the practical point of view, it is especially interesting to assess accuracy, precision and spatial resolution in the presence of strain gradients. Although the radius of the inner part of the scanning electron probe suggests a spatial resolution of approximately 1 nm [7, 15, 8], evaluations of simulations in our previous publication [9] have shown, that especially at sharp interfaces between regions with different lattice plane spacings artefacts occur in the measured strain profiles. These artefacts have been explained in detail by the fact that outer parts of the electron beam (the tails) leak into parts of the sample with a different lattice plane spacing. These tails are expected to have more influence on the measurement of strain if a pattern is imprinted into the condenser aperture [9].

In this study, the accuracy of strain analysis by NBED is considered at interfaces between regions with different lattice plane spacing by evaluation of simulations using various patterns for the condenser aperture. Observations on improved strain precision reported in literature [8, 22] are confirmed. More importantly, it is shown, that the spatial resolution and hence the accuracy of the measurement at interfaces suffers strongly from a pattern in the condenser aperture. This effect is explained by use of our previously published model [9] which has been taken up recently by Yuan et al. [15]. A solution to this problem which is based on geometric phase analysis (GPA) [4] ptychography is provided.

Ptychography as investigated in this report allows for a reconstruction of phase information of the electron wave, which is initially lost because only intensities can be recorded directly in a TEM. Although the principle of ptychography is known for quite a long time [30, 31, 32] its application for STEM has become more important during the last few years [33, 34, 35] benefiting strongly from the development of suitable hardware for the acquisition of 4D-STEM data sets [23, 24, 25, 26, 27]. There are various ptychography methods [36, 37, 38, 39], in this report the extended ptychographical iterative engine (ePIE) [36] is investigated. As in this method object and probe are reconstructed simultaneously, the object can be reconstructed without influence of the probe tails, allowing for a more accurate measurement of strain at interfaces. The phase of the reconstructed sample is further investigated by GPA in order to measure strain.

Details of simulations and methods are presented in Sec. 2, the results are provided and discussed in Sec. 3 and 4, respectively, and a conclusion is given in Sec. 5.

2. Simulations and Methods

2.1. Simulations

The accuracy of measurements of strain at interfaces is investigated by evaluation of simulations. Details of the simulations are provided in this section.

Figure 1: Simulated condenser apertures. From left to right: Standard circular aperture, standard aperture with a cross in the center, bullseye aperture (4 rings), bullseye aperture (8 rings), ray aperture. The last three apertures are inspired by Zeltmann et al. [8].

All simulations have been calculated using multislice simulation routines in the STEMsim code [40] and further MATLAB based extensions. They have been performed aiming at representing experimental measurements on an FEI Titan 80/300 TEM/STEM microscope operated at $U = 300\,\mathrm{kV}$. For NBED the constants for spherical aberration of the probe forming lens and defocus have been

set to $C_S = 1.2\,\text{mm}$ and $\Delta f = -4.7\,\text{nm}$, respectively, and a semi-convergence angle of $\beta = 2.8\,\text{mrad}$ has been used resulting in a probe width of 860 pm (measured as diameter of first ring with zero beam intensity). For GPA-ptychography, Scherzer conditions ($\Delta f = -48.6\,\text{nm}$ and $\beta = 9\,\text{mrad}$) corresponding to a value of $C_S = 1.2\,\text{mm}$ have been applied resulting in a probe width of 260 pm. NBED measurements have been simulated using different shapes of the C2 condenser aperture. These apertures are shown in Fig. 1. The first aperture is a conventional circular aperture, the second one includes an additional cross and is similar to the aperture which was investigated experimentally in Ref. [21] and theoretically in Ref. [9]. But in contrast to Ref. [9] it is rotated with respect to the crystal main axes. The remaining three apertures are inspired by the apertures of Zeltmann et al. [8]. To account for experimental effects during the recording process of the diffraction patterns the protocol of Grieb et al. [20] has been applied to the simulated diffraction patterns. Therefore, shot noise according to an electron beam current of $I = 60\,\text{pA}$ [41] and a camera frame time of $t = 100\,\text{ms}$ (NBED measurements) or rather $t = 10\,\text{ms}$ (ptychography) has been applied to the simulations. Furthermore, for NBED measurements contrast and intensity have been rescaled and the modulation transfer function (MTF) of a Gatan Ultra Scan 2000 CCD camera [42] has been applied.

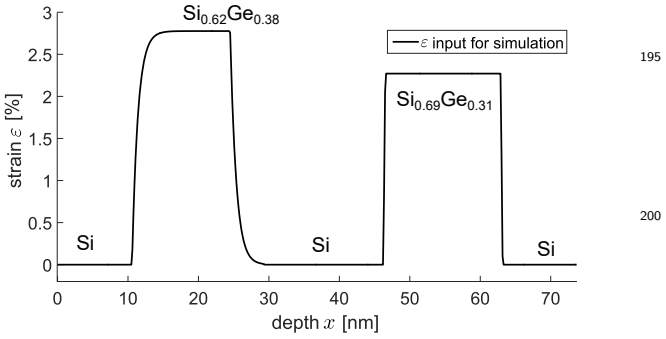

Figure 2: Strain of the simulated model structure. The sample consists of two SiGe quantum wells with different Ge concentrations (indicated by subscripts) which are embedded in pure Si. The left quantum well shows a segregation profile.

Simulations are carried out assuming a silicon-germanium (SiGe) sample as already used in previous publications [9, 22], which is similar to an experimental sample, that has been investigated in detail [22, 43, 13, 10]. It consists of two SiGe-quantum wells, with germanium (Ge) concentrations of 38 % and 31 % embedded in pure silicon (Si). The first quantum well shows a segregation profile according to the model of Muraki et al. [44] with a Ge segregation efficiency of $R = 72\,\%$ [45], the second quantum well shows a sharp rectangular profile. Fig. 2 depicts the resulting strain profile.
Two samples with thicknesses of 50 nm and 1 nm have been simulated. In both cases the crystal consists of 145 unit-cells in [001] growth-direction, which corresponds to the direction with the resulting strain profile in Fig. 2. The crystal is viewed in [110] zone axis orientation. The resulting diffraction discs have a diameter of 92 px for NBED. If electron beam precession is used, diffraction patterns were simulated using $N = 32$ different equally spaced tilt directions with a tilt angle of $\alpha = 0.5\,°$. As for the simulated sample strain varies only along one spatial dimension, simulations of linescans are sufficient to measure strain by NBED. Hence, linescans with a length of 73.6 nm consisting of 200 diffraction patterns were simulated for NBED corresponding to a scanning step size of 0.37 nm. For GPA-ptychography a two-dimensional area scan with a smaller scanning step size is necessary to be able to reconstruct the object. Therefore, an area scan with a size of $73.9\,\text{nm} \times 3.8\,\text{nm}$ consisting of 945×50 diffraction patterns was calculated corresponding to a scanning step size of 77 pm.
GPA-ptychography and NBED precession measurements have been simulated in the absorptive-potential approach [46, 47], NBED simulations without precession have been calculated in the frozen-lattice approach [48]. In this case, intensities of 14 simulated diffraction patterns, each simulated with a different, statistical, Gaussian distributed displacement of the atoms have been averaged. Displacements have been calculated according to the Debye-Waller factor at $T = 300\,\text{K}$ [49]. A simulated diffraction pattern for NBED measurements without precession is shown exemplary in Fig. 3.

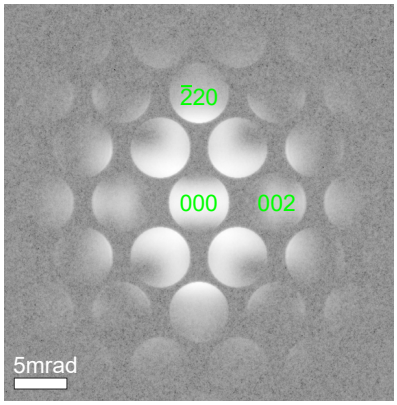

Figure 3: Simulated diffraction pattern for NBED measurements. The pattern was simulated in pure silicon with a sample thickness of 50 nm viewed in [110] zone axis orientation without precession.

2.2. Methods

Two methods are investigated and compared in terms of their accuracy of measured strain at interfaces, namely strain analysis by nano-beam electron diffraction and GPA-ptychography. A methodical summary of these methods is given in the following section. Both methods evaluate 4D-STEM data sets.

2.2.1. Strain analysis by nano-beam electron diffraction

For strain analysis by NBED distances between diffraction discs are evaluated. For this reason, the convergence angle of the probe is chosen such that diffraction discs do not overlap. Measuring distances $\vec{g}_1$ and $\vec{g}_2$ between diffraction discs in two linearly independent directions and comparing them to distances $\vec{g}_1^0$ and $\vec{g}_2^0$ in diffraction patterns acquired in an unstrained reference region of the sample allows for a determination of the relative lattice plane spacing ε which is called strain here [50]:

$$\begin{aligned}\mathbb{G} &= \begin{bmatrix} g_{1x} & g_{2x} \\ g_{1y} & g_{2y} \end{bmatrix}; \quad \mathbb{G}_0 = \begin{bmatrix} g_{1x}^0 & g_{2x}^0 \\ g_{1y}^0 & g_{2y}^0 \end{bmatrix} \\ \mathbb{D} &= (\mathbb{G}^{\mathrm{T}})^{-1}\mathbb{G}_0^{\mathrm{T}} - \mathbb{I} \\ \varepsilon &= \frac{1}{2}\cdot\left(\mathbb{D}+\mathbb{D}^{\mathrm{T}}\right) = \begin{bmatrix} \varepsilon_1 & \varepsilon_{1,2} \\ \varepsilon_{2,1} & \varepsilon_2 \end{bmatrix}. \end{aligned} \tag{1}$$

Here $\mathbb{I}$ is the identity matrix, ε_1 describes the strain along direction $\vec{d}_1$, ε_2 is the strain along direction $\vec{d}_2$, $\varepsilon_{1,2} = \varepsilon_{2,1}$ is the shear strain and $\vec{d}_{1,2}$ are the real space lattice vectors corresponding to the reciprocal vectors $\vec{g}_{1,2}$.

To measure distances between discs, their positions have to be determined accurately and precisely. Many different techniques have been suggested and investigated in literature, the first category of techniques relies on a correlation of patches around the diffraction discs $I_{\mathrm{image}}(\vec{k})$ with suitable masks $I_{\mathrm{mask}}(\vec{k})$ [12, 7, 8]. Using Fourier transforms correlation maps $I_{\mathrm{corr}}(\vec{k})$ can be calculated by

$$\begin{aligned} G_{\mathrm{image}}(\vec{s}) &= \mathcal{F}\{I_{\mathrm{image}}(\vec{k})\} \\ G_{\mathrm{mask}}(\vec{s}) &= \mathcal{F}\{I_{\mathrm{mask}}(\vec{k})\} \\ I_{\mathrm{corr}}(\vec{k}) &= \mathcal{F}^{-1}\left\{ \frac{G_{\mathrm{image}}(\vec{s})\cdot G^*_{\mathrm{mask}}(\vec{s})}{|G_{\mathrm{image}}(\vec{s})\cdot G^*_{\mathrm{mask}}(\vec{s})|^p} \right\} \quad . \end{aligned} \tag{2}$$

Cross-correlation is calculated for $p = 0$, phase-correlation is calculated for $p = 1$ and for $0 < p < 1$ a hybrid solution is obtained [19, 8]. A value of $p = 0$ yielded the best results for the evaluations shown in this report. The shift between mask and image is calculated from the maximum in the correlation map, which can be determined with subpixel accuracy using polynomial fits to the maximum or numerical upsampling of image and mask.

The second category of disc position determination techniques is based on edge detection. Edges in patches containing the diffraction disc can be determined using mathematical filters. Subsequently, position and radius of the diffraction disc can be determined with iterative circle fitting algorithms [7] or using circular Hough transforms [15].

A third technique is based on the maximization of radial gradients [7, 18]. Two sets of rings are positioned in a patch containing the diffraction disc. The first set has larger radii (ranging from 100 % to 120 % of the expected disc radius) and the second set has smaller radii (ranging from 80 % to 100 % of the expected disc radius). Image intensities touched by the rings are integrated for both sets separately. Center position of all rings and expected disc radius are varied until the difference between both integrated intensities is at maximum. In this case, the smaller set of rings is positioned inside the diffraction disc and the larger set of rings is positioned outside the disc. Details are given in Ref. [7].

All techniques can be extended by fitting a regular lattice to all diffraction disc positions or by fitting all disc positions simultaneously [17, 19, 18, 15, 8].

2.2.2. Geometric phase analysis ptychography

The extended ptychographical iterative engine (ePIE) [36] is investigated in terms of its applicability for measurements of strain. With ePIE, the complex object function $O(\vec{r})$ as well as the complex probe function $P(\vec{r})$ are reconstructed iteratively. All diffraction patterns of the 4D-STEM data set are considered in a random order $s(j)$. Starting ($j = 1$) with an initial guess for $O_j(\vec{r})$ and $P_j(\vec{r})$, a first exit wave $\Psi_j(\vec{r})$ is calculated within the object function approximation by

$$\Psi_j(\vec{r}) = O_j(\vec{r})P_j(\vec{r} - \vec{R}_{s(j)}) \quad , \tag{3}$$

where $\vec{R}_{s(j)}$ is the position of the probe on the object for the acquisition of diffraction pattern $I_{s(j)}(\vec{k})$. Following the protocol of Maiden et al. [36] the amplitude of the Fourier transform of this exit wave is replaced by the positive square-root of the recorded $s(j)$-th diffraction pattern according to

$$\Psi_j(\vec{k}) = \sqrt{I_{s(j)}(\vec{k})}\frac{\mathcal{F}\{\Psi_j(\vec{r})\}}{|\mathcal{F}\{\Psi_j(\vec{r})\}|} \tag{4}$$

and an updated exit wave $\Psi'_j(\vec{r})$ is calculated by inverse Fourier transform. Updated object $O_{j+1}(\vec{r})$ and probe $P_{j+1}(\vec{r})$ functions are than obtained by

$$\begin{aligned} &O_{j+1}(\vec{r}) \\ &\quad = O_j(\vec{r}) + \frac{\alpha\cdot P_j^*(\vec{r}-\vec{R}_{s(j)})}{\left|P_j(\vec{r}-\vec{R}_{s(j)})\right|^2_{\max}}\left(\Psi'_j(\vec{r}) - \Psi_j(\vec{r})\right) \end{aligned} \tag{5}$$

$$\begin{aligned} &P_{j+1}(\vec{r}-\vec{R}_{s(j)}) \\ &\quad = P_j(\vec{r}-\vec{R}_{s(j)}) + \frac{\beta\cdot O_j^*(\vec{r})}{|O_j(\vec{r})|^2_{\max}}\left(\Psi'_j(\vec{r}) - \Psi_j(\vec{r})\right) \quad . \end{aligned} \tag{6}$$

The update step-size parameters α and β have been set to $\alpha = \beta = 1$ for the results presented in this report. Subsequently, the procedure is repeated with the next diffraction pattern of the data set. The ptychography reconstructions in the present report have been performed with a self-written MATLAB based software.

Once the complex exit wave is reconstructed, the same

methods for measurements of strain can be applied, as have been used to evaluate conventional TEM or STEM images for a very long time. For the evaluations shown in this report, the phase of the reconstructed object (called 'image' in the following part) is further considered for the measurements of strain.

GPA is one of these methods, details can be found in Ref. [4]. Briefly, a mask is applied to the Fourier transform (diffractogram) of the image. This mask selects one peak in the diffractogram. Shifting this peak back to the center of the diffractogram and calculating the inverse Fourier transform results in a complex image, whose phase is called the geometric phase. This procedure is repeated for a second peak in the diffractogram, whose direction towards the image center is linearly independent to the direction of the previous peak. From the gradients in the geometric phase, strain along directions selected by the peaks can be measured according to Ref. [4].

The shape of the mask which is applied to the diffractogram can have a strong influence on the quality of the measured strain profile. The size of the mask determines the spatial resolution, the sharpness of the mask can cause artefacts in the measured profile. For the measurements shown in this report, a circular mask with a diameter equal to the distance between two neighbouring peaks is used. Parts of the mask with a radius $> 95\%$ of the complete radius are damped from 1 to 0 with a cosine-like shape.

3. Results

Results of this report are divided into three parts. In Sec. 3.1 precision, accuracy and broadening are compared evaluating simulations using various condenser apertures. In Sec. 3.2 the results are explained and in Sec. 3.3 a solution for improved measurements of strain at interfaces is provided.

3.1. Precision and accuracy at interfaces using patterned apertures

Throughout this paper we use simulated diffraction patterns to investigate the effect of different condenser apertures on precision and accuracy of measurements of strain at interfaces. The phrase *measured strain profile* is therefore related to the evaluation of simulated data, carried out in the same way as would be done with experimental diffraction patterns. To quantify the quality of measured strain profiles three different parameters have to be defined. For precision σ and accuracy Δ we keep the definitions of a previous publication [9]. The precision is defined as standard deviation of measured values in the strain-free reference region. The accuracy is defined as the difference between the average measured strain and the true strain in a region with constant strain. To compare the broadening of the measured profile and hence the accuracy at interfaces, a new measure is defined, which is obtained from the left part of the sharp quantum well in Fig. 2. An error function of the following form is fitted to the step edge in the strain profile between $x = 36.6\,\mathrm{nm}$ and $x = 55.1\,\mathrm{nm}$:

$$\varepsilon(x) = a \cdot \mathrm{erf}\left(\frac{x - x_0}{\kappa}\right) + c \quad , \tag{7}$$

where erf is the error function, x is the position in the strain profile, a and c are fit parameters that determine the height of the fitted step edge and x_0 is a fit parameter that determines the position of the edge. The most important fit parameter for this report is the parameter κ that scales the error function along x. Therefore, it is a measure for the broadening of the measured step edge. The smaller the value of κ the more accurate is the evaluated profile. For all NBED evaluations shown in this report, distances between (004) and $(00\bar{4})$ diffraction disc were evaluated.

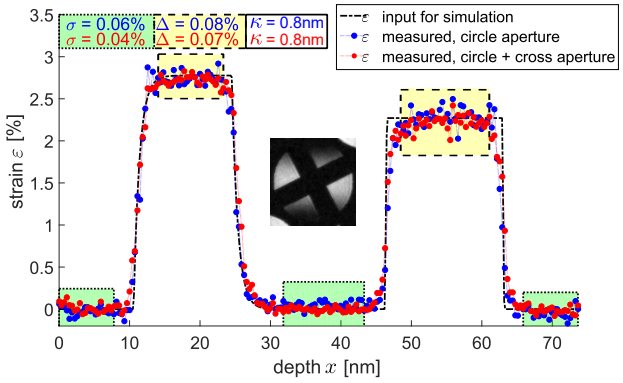

Figure 4: Comparison of simulated strain profile (black curve) with evaluated strain. Blue curve: evaluation of simulation with the standard circular aperture, red curve: evaluation of simulation with a circular aperture with additional cross (see inset). Simulations without precession. Green marked regions show parts in which the precision σ is determined, yellow marked regions show parts in which the accuracy Δ is determined. Analysis with the aperture including a cross is more precise and accurate.

In Fig. 4 the true strain (black curve) is compared to the measured strain evaluating a simulation with a circular aperture (blue curve) and a simulation with a circular aperture with an additional cross (red curve). The inset depicts a patch of the diffraction pattern mainly showing the primary beam. Regions from which the precision σ is calculated are marked in green, regions from which the accuracy Δ is calculated are marked in yellow. Both simulations have been calculated without electron beam precession. The evaluation of the simulation with a circular aperture has been performed with the radial gradient technique (see Sec. 2.2.1), the evaluation of the simulation with additional cross in the aperture has been performed using the cross-correlation technique with an image of the simulated aperture as mask, as these two techniques yielded the best results for the evaluation of these two different simulations.

Comparison of precision and accuracy for both apertures

confirms the result of Zeltmann et al. The precision of $\sigma = 0.04\,\%$ using the aperture including a cross is better than the value of $\sigma = 0.06\,\%$ using the conventional aperture. Also the accuracy is slightly better. Qualitatively, both profiles agree with the true strain profile, which is in accordance with the experimental results in Ref. [21]. The fitted values for the broadening parameter κ reveal $\kappa = 0.8\,\mathrm{nm}$ for both apertures.

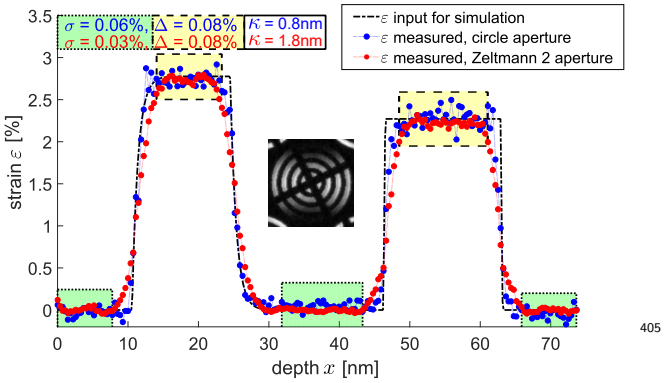

Figure 5: Comparison of simulated strain profile (black curve) and evaluated strain. Blue curve: evaluation of simulation with the standard circular aperture, red curve: evaluation of simulation with a bullseye shaped aperture Zeltmann 2 (see inset). Simulations without precession. Green marked regions show parts in which the precision σ is determined, yellow marked regions show parts in which the accuracy Δ is determined. Analysis with the bullseye aperture Zeltmann 2 is more precise, but edges of the profile appear blurred compared to the analysis with the standard aperture.

A different conclusion must be drawn from the evaluation shown in Fig. 5. Here, the true strain profile (black curve) is compared to evaluations of simulations with the standard circular aperture (blue curve) and the bullseye aperture Zeltmann 2 (red curve). An image of the primary beam is shown as inset. Evaluation of the simulation with the Zeltmann 2 aperture has been performed using the cross-correlation technique with an image of the simulated aperture as mask. The precision of $\sigma = 0.03\,\%$ is by a factor of 2 better than the precision using the conventional aperture confirming the results of Zeltmann et al. [8]. Accuracies Δ are the same for both apertures. A look at the interface reveals the important difference. The strain profile measured evaluating the simulation with the Zeltmann 2 aperture is blurred compared to the true strain profile and compared to the evaluation using the conventional aperture. Fitted broadening parameters of $\kappa = 1.8\,\mathrm{nm}$ for the Zeltmann 2 aperture and $\kappa = 0.8\,\mathrm{nm}$ for the conventional aperture confirm this impression quantitatively. This shows that although the accuracy in the center of the quantum well is the same for both apertures, the measured strain at the interface is less accurate using the Zeltmann 2 aperture.

This result is further confirmed by the summary in Tab. 1. Precisions σ of all evaluations of simulations without electron beam precession are better for simulations with a patterned condenser aperture confirming the results of Zeltmann et al. [8]. The accuracies Δ are very similar, slightly better for patterned apertures. But the more detailed the pattern in the aperture is, the more increases the broadening of the measured profile. It is worst for the aperture Zeltmann 2 ($\kappa = 1.8\,\mathrm{nm}$), which has the most patterned structure (compare Fig. 1). An explanation is given in Sec. 3.2.

Table 1: Comparison of quality of measured strain evaluating simulations using various condenser apertures. Simulations without precession using a sample with a thickness of 50 nm. The precisions σ are better for apertures with a pattern, the accuracies Δ are very similar, whereas the broadening κ is worse for patterned apertures compared to the conventional circular aperture.

aperture	σ	Δ	κ
circle	0.06 %	0.08 %	0.8 nm
circle + cross	0.04 %	0.07 %	0.8 nm
Zeltmann 1	0.03 %	0.06 %	1.0 nm
Zeltmann 2	0.03 %	0.08 %	1.8 nm
Zeltmann 3	0.03 %	0.06 %	1.1 nm

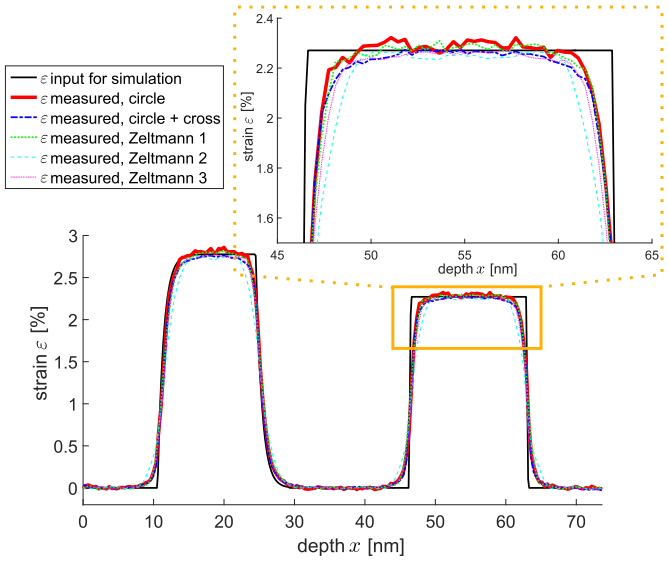

Figure 6: Comparison of true strain profile (black curve) and measured strain evaluating simulations using various condenser apertures. Simulations with precession. Patterns of the apertures are shown in Fig. 1. Evaluations with the cross-correlation technique. Inset shows the magnified upper part of the second SiGe-quantum well. Qualitatively, all measured profiles with patterned probes appear blurred compared to the evaluation of the simulation using the standard circular aperture (red curve).

Electron beam precession has been found to be the key improving the precision of measurements of strain [13, 9]. For this reason, evaluations of simulations with various condenser apertures using precession are compared in Fig. 6. Simulations have been evaluated using the cross-

correlation technique. For patterned apertures the apertures have been used as a mask, for the conventional circular aperture a ring mask with an inner radius of 80 % of the actual radius yielded the best result. In general, the true strain profile (black curve) is recovered from all simulations quite well, independent of the simulated aperture. Differences can be seen only at the interfaces. An example is shown magnified as inset. The broadening κ depends on the pattern of the aperture used in the simulation.

Table 2: Comparison of quality of measured strain evaluating simulations using various condenser apertures. Simulation with precession using a sample with a thickness of 50 nm. The precisions σ are equal, whereas accuracies Δ and broadening parameters κ are worse for patterned apertures.

aperture	σ	Δ	κ
circle	0.01 %	0.02 %	1.0 nm
circle + cross	0.01 %	0.03 %	0.9 nm
Zeltmann 1	0.01 %	0.02 %	1.2 nm
Zeltmann 2	0.01 %	0.05 %	1.7 nm
Zeltmann 3	0.01 %	0.03 %	1.2 nm

Quantitatively, this result is confirmed in Tab. 2. Precisions are independent of the condenser aperture $\sigma = 0.01\,\%$. Accuracies Δ and broadening parameters κ are worse for patterned apertures compared to the conventional circular aperture. There is one exception: the circular aperture with additional cross has a better broadening parameter of $\kappa = 0.9\,\text{nm}$ compared to the conventional aperture ($\kappa = 1.0\,\text{nm}$). But as the accuracy is worse for the aperture with additional cross ($\Delta = 0.03\,\%$ for the aperture with additional cross compared to $\Delta = 0.02\,\%$ for the conventional aperture), it can be concluded that both apertures allow for measurements of strain with a similar quality.

A further result can be concluded from the comparison of individual values for κ in Tab. 1 (without electron beam precession) to the corresponding values in Tab. 2 (with electron beam precession). The broadening parameter is larger for almost all evaluations with precession and hence the measured profile is sharper if electron beam precession is not used. This can be explained by the fact that using precession the electron beam hits the sample with a tilt angle of $\alpha = 0.5\,^\circ$ which causes beam broadening effects within the sample [9].

In conclusion, the best quantitative result in terms of precision, accuracy and broadening is still obtained with a conventional circular condenser aperture in combination with electron beam precession.

Recently, Yuan et al. suggested edge detection in combination with a circular Hough transform as a technique for precise disc position determination [15]. This technique has also been applied to simulations in this report including electron beam precession. For edge detection a *Laplacian of Gaussian* filter [51] yielded the best result.

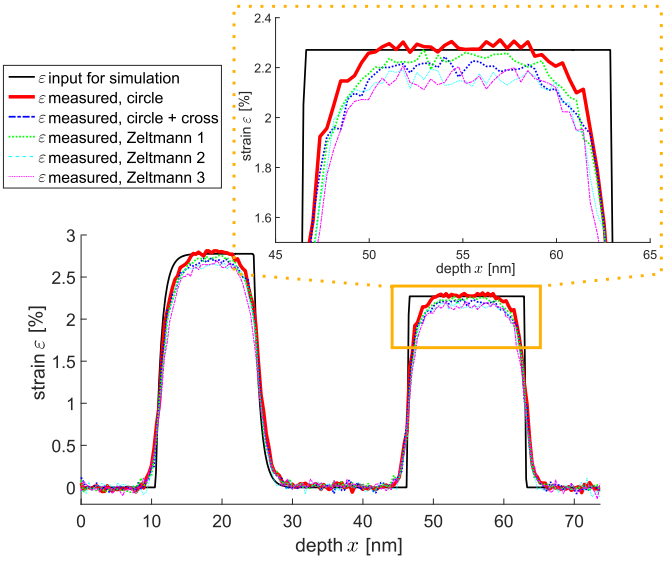

Figure 7: Comparison of true strain profile (black curve) and measured strain evaluating simulations using various condenser apertures. Simulations with precession. Patterns of apertures shown in Fig. 1. Evaluation using edge detection and a circular Hough transformation. Inset shows the magnified upper part of the second SiGe-quantum well. Qualitatively, all measured profiles with patterned probes appear more blurred compared to the evaluation of the simulation using the standard circular aperture (red curve).

The result is shown for evaluations of simulations with various condenser apertures in Fig. 7 in comparison to the true strain profile (black curve). The inset shows a magnified part of the measurement. Once again, the best result in terms of accuracy ($\Delta = 0.04\,\%$) and broadening ($\kappa = 1.3\,\text{nm}$) is obtained by evaluation of the simulation with the conventional circular condenser aperture (red curve). The precisions of all evaluations are between $\sigma = 0.03\,\%$ and $\sigma = 0.04\,\%$ and hence worse than the values shown in Fig. 6 and Tab. 2 using the cross-correlation technique for the evaluation.

Finally, the auto-correlation based technique suggested by Guzzinati et al. [22] has been applied to evaluate the simulations with precession. To this end, auto-correlation maps of individual diffraction patterns were calculated and reciprocal lattice vectors were obtained from peak positions in these maps. The result is shown in Fig. 8. None of the evaluations shows a sharp strain profile. The best value for the broadening is obtained for the conventional circular aperture reaching a value of $\kappa = 1.2\,\text{nm}$, the worst value of $\kappa = 2.2\,\text{nm}$ is obtained for the aperture Zeltmann 2. This indicates that condenser apertures with a pattern do not improve the quality of the measured strain profile using the auto-correlation technique.

3.2. Explanation

In the preceding section it has been shown that the broadening of measured strain profiles and hence the accuracy at interfaces is worse if patterned condenser apertures

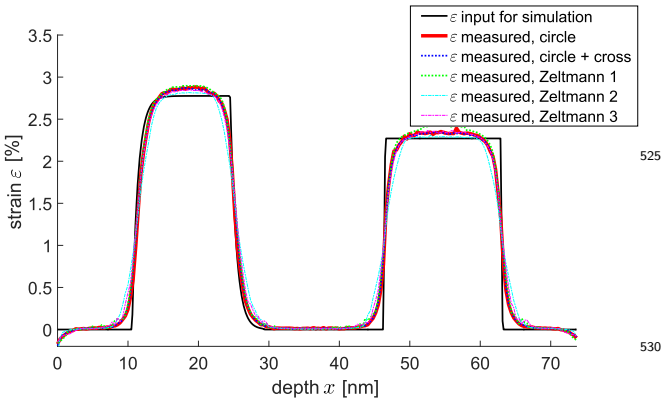

Figure 8: Comparison of true strain profile (black curve) and measured strain evaluating simulations using various condenser apertures. Simulations with precession. Patterns of apertures shown in Fig. 1. Evaluation using an auto-correlation of the simulated diffraction patterns. Independent of the aperture all measured profiles appear blurred compared to the true strain profile.

are used compared to the conventional circular aperture. The reason for this effect is the extent of the electron probe (its tails) which is scanned across the sample. This effect has been explained in a previous publication [9], it is emphasized here for completeness. The probe wave function can be described as inverse Fourier transform of the wave function in the condenser aperture plane. Sharp edges of the aperture are represented by contributions at high spatial frequencies in the Fourier transform and hence in the tails of the electron probe. The more sharp edges the aperture has the more contributions exist in the tails of the electron probe.

If the scanning probe approaches an interface between regions with different lattice plane spacing, parts of its tails pass the sample at the other side of the interface than the central part of the probe. For these electrons the Bragg condition for constructive interference is fulfilled under a different diffraction angle compared to the electrons in the central part of the probe. For this reason, parts of the edges of the diffraction discs in the diffraction pattern appear shifted as *halos* [9] with respect to the major parts of the discs. The more electrons contribute to the tails the more of the diffraction disc is shifted with respect to the major part of the disc. And hence, the more patterned the aperture is the more of the diffraction disc is shifted towards the position expected when the central part of the probe is positioned at the other side of the interface. Disc detection algorithms applied to these diffraction discs see both parts: parts of the disc at the true position and shifted parts of the disc. This results in broader peaks in the correlation maps or in the Hough transformation. These broader peaks are then fitted with a polynomial [7] or a Lorentzian [15] in order to reach subpixel accuracy. But the more parts of the disc are shifted the more the maxima in the correlation maps appear shifted when fitted by e.g. polynomials. This results in a blur of the measured profile. Hence the result can be concluded as follows: more patterned apertures lead to more contributions in the tails of the probe, which leads to more shifted parts of the diffraction discs, yielding broader and more shifted maxima in the correlation maps and finally this results in a higher amount of blurring of the measured strain profile.

3.3. Improved measurement of strain at the interface

A possibility to avoid this effect has been suggested in Ref. [9]. Using apertures without sharp edges and hence less contributions in the tails of the electron probe can minimize this effect. This has been proven by evaluation of simulations using an aperture with a Gaussian shape. But an aperture without sharp edges is not easy to produce and it causes other problems [9].

Here, a different solution is suggested. Complex object and probe functions can be reconstructed by ptychography. This is illustrated in Fig. 9, where a comparison between the complex input values for the simulation (Fig. 9a)-c)) and the corresponding reconstructed complex values (Fig. 9d)-f)) is provided. In general, there is a good agreement between simulation input and reconstructed values. Furthermore, an example diffraction pattern is presented in Fig. 9g).

As the tails of the probe are part of the electron probe, the object should be reconstructed without effects of the probe tails. To investigate this, strain was measured from the ptychographically reconstructed object by GPA.

The result is shown in Fig. 10. True strain (black curve) is compared to evaluated strain using precession NBED (red curve) as well as to evaluated strain obtained by GPA-ptychography (blue curve). For the GPA measurement the (004) peak in the diffractogram was selected. It is obvious that the GPA-ptychography profile is sharper than the NBED profile. The values of $\kappa = 0.4\,\mathrm{nm}$ for GPA-ptychography and $\kappa = 0.9\,\mathrm{nm}$ for NBED confirm this result quantitatively. However, it is important to note, that in this special case two simulations for a very thin (1 nm) sample are compared as ptychography reconstructions in the form as used for this report succeed only for thin samples.

4. Discussion

It is an idea of this report that GPA-ptychography is a promising alternative for accurate measurements of strain at interfaces. But it has to be pointed out that this result has to be considered only as a proof of principle. The ptychography reconstruction has been performed evaluating a simulation of a sample with a thickness of only 1 nm. The reason for this is that the ptychography algorithm investigated in this report, relies on an object function approximation as the whole interaction of probe and object is described mathematically by only one single multiplication (see Sec. 2.2.2) [33]. Therefore, it cannot simply be applied to thick samples. For thick samples as the ones used

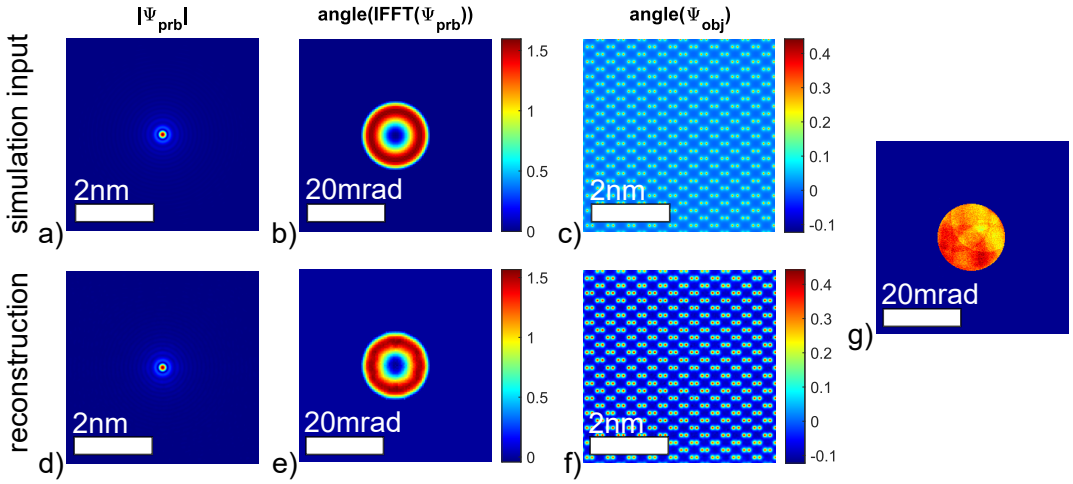

Figure 9: Comparison of simulation input and ptychography reconstruction. a) and d) absolute value of the probe, b) and e) phase of inverse Fourier-transform of the probe, c) and f) phase of the object, g) example diffraction pattern.

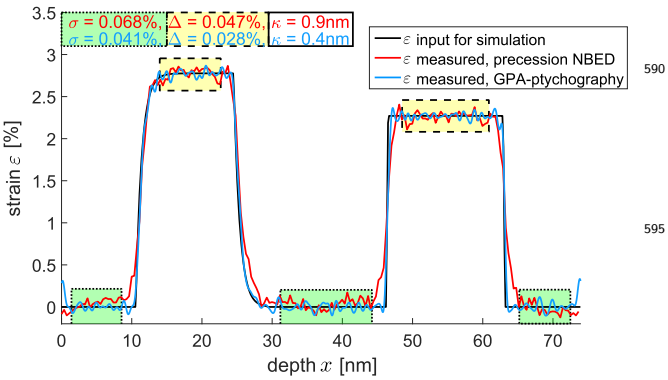

Figure 10: Comparison of true strain profile (black curve) and measured strain evaluating simulations using precession NBED (red curve) and GPA-ptychography (blue curve). Green marked regions show parts in which the precision σ is determined, yellow marked regions show parts in which the accuracy Δ is determined. Evaluation using GPA-ptychography recovers the true shape of the strain profile more exactly compared to the NBED analysis. For both measurements the (004) peak in the diffractogram or the (004) disc in the diffraction pattern were evaluated.

for the majority of the NBED simulations or for real experimental samples inverse multislice reconstructions [52, 53] could be a solution. Furthermore, it is expected that also sampling rates of diffraction patterns and reconstructed object as well as the scanning step size could have an impact on the quality of the reconstructed strain profile [54]. This is subject to future research.

It could be assumed that application of GPA to conventional (S)TEM images reveals a similar quality of the measured strain profile compared to GPA-ptychography. The advantage of application to the reconstructed object function over the application to (S)TEM images is that in ptychography the field of view is in principal unlimited as long as a sufficiently large number of diffraction patterns can be stored and processed during the reconstruction process, whereas in (S)TEM the field of view is limited to a few tens of nanometres due to effects such as sample bending and focus variation. Furthermore, the ptychographically reconstructed object is less affected by lens aberrations because aberrations are reconstructed mainly in the probe function [33, 54].

Values determined for the broadening κ cannot be used to determine the spatial resolution of the NBED method. They can only be used to compare the quality of similar evaluations. The reason for this can be seen as follows. For the NBED evaluations shown in this report distances between (004)- and (00$\overline{4}$)-diffraction discs have been evaluated. Evaluating the simulation with the standard circular aperture and electron beam precession, this revealed a broadening of $\kappa = 1.0\,\mathrm{nm}$. But an evaluation of distances between (002)- and (00$\overline{2}$)-diffraction discs reveals a value of $\kappa = 1.5\,\mathrm{nm}$ for the same simulation. The reason for this difference is that disc position in the strain-free region and disc position in the strained region are closer to each other for (002)-diffraction discs compared to (004)-diffraction discs. For the (002)-disc the true disc and the partially shifted disc are melted into one single object whereas they can be separated by eye for (004)-diffraction discs. Hence, effects of partially shifted discs caused by probe tails have a stronger influence on the detection of (002)-diffraction disc positions. For this reason, the broadening parameter κ can only be used to compare evaluations of simulations in which distances between the same diffractions discs are evaluated. In general, it is beneficial to evaluate distances between high index diffraction discs as long as they are excited homogeneously without that the sample has to be tilted [21].

A similar argument holds for precision σ and accuracy Δ. Exact numerical values for both depend on the simulation.

In this report linescans including 200 diffraction patterns have been simulated on a 50 nm thick sample, whereas in a previous publication only 100 patterns per linescan were simulated on the same sample structure with a thickness of only 25 nm [9]. For this reason, the exact values for σ and Δ are numerically different. Simulating a different sample or changing the number of pixel per diffraction disc can also have an impact on the numerical values of σ and Δ. The values for the precision and accuracy can only be compared directly if only one parameter such as the pattern of the condenser aperture is different.

In a previous publication it was shown that strain evaluations of simulations with a circular aperture with additional cross have a worse quality than evaluations of simulations with the conventional aperture [9]. In the present publication it has been shown that the measurement using the aperture with additional cross has the same quality as a measurement with a circular aperture if electron beam precession is used. For measurements without precession the aperture with additional cross reveals a better result than the conventional aperture. There are two main reasons that explain this difference. Firstly, in Ref. [9] neither noise nor the MTF have been applied to the simulations that compare various apertures, whereas in the present report these effects have been included. Secondly, the aperture with additional cross used in the present report is rotated with respect to the aperture used in Ref. [9]. This is beneficial because in this manner the cross is not aligned to the simulation grid. Otherwise, aliasing effects could occur according to Ref. [8]. To emphasize, an aperture with additional cross improves the precision of measurements of strain if electron beam precession is not available.

To exclude that the blur of measured strain profiles is only a beam broadening effect within the sample, the NBED linescan on a 1 nm thin sample is compared here to the linescan on a 50 nm thick sample shown in Figs. 4 and 5. Noise in only faintly excited diffraction discs is the reason for a worse precision of $\sigma = 0.07\,\%$ (thin sample) compared to the thick sample ($\sigma = 0.06\,\%$). The broadening parameter of $\kappa = 0.9$ nm for the thin sample compared to $\kappa = 0.8$ nm for the thick sample is worse for the thin sample, which confirms that the blur of the measured profile is not a beam broadening effect, for further results on beam broadening see Ref. [21].

Finally, it could not be confirmed that diffraction disc position detection using edge detection based Hough transformations as suggested by Yuan et al. [15] improves the quality of the strain measurement. It has to be pointed out that evaluation of simulations using Hough transformations succeeds only if diffraction discs are illuminated homogeneously. This means that very thin samples or electron beam precession have to be used, otherwise the Hough transformation fails in determining the true disc position, especially in diffraction patterns acquired close to sharp interfaces. Furthermore, the precision is worse compared to evaluations using cross-correlation based techniques.

5. Conclusion

The accuracy of strain measured at interfaces between regions with different lattice plane spacing using NBED has been investigated by evaluations of simulations. It has been found that a pattern in the condenser aperture significantly improves the precision of the measurement confirming previous results [8]. If electron beam precession is available a pattern in the condenser aperture yields no improvement of the precision. More important, it is shown that using patterned condenser apertures the broadening of measured strain profiles and hence the accuracy at the interface is significantly worsened compared to measurements using the conventional circular aperture. The effect has been explained by tails of the scanning electron probe leaking in regions of the sample with a different strain state. These tails have a stronger impact on the measurement the more patterns are imprinted to the condenser aperture. As a proof of principle it is shown that GPA-ptychography provides a solution to this problem. This method allows for a more accurate measurement of strain at interfaces because the sample can be reconstructed without influence of probe tails.

Acknowledgements

This work was supported by the Deutsche Forschungsgemeinschaft (DFG) under contract no. RO2057/12-2 within the research unit FOR2213 (www.nagocat.de) and under contract no. RO 2057/16-1. KMC acknowledges funding from the Helmholtz Society under contracts VH-NG-1317 and ZT-I-0025.

References

[1] W. Bernard, W. Rindner, H. Roth, Anisotropic Stress Effect on the Excess Current in Tunnel Diodes, Journal of Applied Physics 35 (6) (1964) 1860–1862. doi:10.1063/1.1713755.

[2] M. Mavrikakis, P. Stoltze, J. Nørskov, Making gold less noble, Catalysis Letters 64 (2) (2000) 101–106. doi:10.1023/A:1019028229377.

[3] J. Coleman, Strained-layer InGaAs quantum-well heterostructure lasers, IEEE Journal of Selected Topics in Quantum Electronics 6 (6) (2000) 1008–1013. doi:10.1016/0040-6090(92)90871-8.

[4] M. Hÿtch, E. Snoeck, R. Kilaas, Quantitative measurement of displacement and strain fields from HREM micrographs, Ultramicroscopy 74 (3) (1998) 131 – 146. doi:10.1016/S0304-3991(98)00035-7.

[5] R. Wittmann, C. Parzinger, D. Gerthsen, Quantitative determination of lattice parameters from CBED patterns: accuracy and performance, Ultramicroscopy 70 (3) (1998) 145 – 159. doi:10.1016/S0304-3991(97)00107-1.

[6] A. Béché, J.-L. Rouvière, L. Clément, J. Hartmann, Improved precision in strain measurement using nanobeam electron diffraction, Applied Physics Letters 95 (12) (2009) 123114. doi:10.1063/1.3224886.

[7] K. Müller, A. Rosenauer, M. Schowalter, J. Zweck, R. Fritz, K. Volz, Strain Measurement in Semiconductor Heterostructures by Scanning Transmission Electron Microscopy, Microscopy and Microanalysis 18 (2012) 995–1009. doi:10.1017/S1431927612001274.

[8] S. E. Zeltmann, A. Müller, K. C. Bustillo, B. Savitzky, L. Hughes, A. M. Minor, C. Ophus, Patterned probes for high precision 4D-STEM bragg measurements, Ultramicroscopy 209 (2020) 112890. doi:https://doi.org/10.1016/j.ultramic.2019.112890.

[9] C. Mahr, K. Müller-Caspary, T. Grieb, M. Schowalter, T. Mehrtens, F. F. Krause, D. Zillmann, A. Rosenauer, Theoretical study of precision and accuracy of strain analysis by nano-beam electron diffraction, Ultramicroscopy 158 (2015) 38 – 48. doi:http://dx.doi.org/10.1016/j.ultramic.2015.06.011.

[10] D. Cooper, T. Denneulin, N. Bernier, A. Béché, J.-L. Rouvière, Strain mapping of semiconductor specimens with nm-scale resolution in a transmission electron microscope, Micron 80 (2016) 145 – 165. doi:https://doi.org/10.1016/j.micron.2015.09.001.

[11] C. Ophus, Four-Dimensional Scanning Transmission Electron Microscopy (4D-STEM): From Scanning Nanodiffraction to Ptychography and Beyond, Microscopy and Microanalysis 25 (3) (2019) 563–582. doi:10.1017/S1431927619000497.

[12] F. Uesugi, A. Hokazono, S. Takeno, Evaluation of two-dimensional strain distribution by STEM/NBD, Ultramicroscopy 111 (8) (2011) 995 – 998. doi:http://dx.doi.org/10.1016/j.ultramic.2011.01.035.

[13] J.-L. Rouvière, A. Béché, Y. Martin, T. Denneulin, D. Cooper, Improved strain precision with high spatial resolution using nanobeam precession electron diffraction, Applied Physics Letters 103 (24) (2013) –. doi:10.1063/1.4829154.

[14] W. Bragg, W. Bragg, The reflection of X-rays by crystals, Proceedings of the Royal Society of London. Series A 88 (605) (1913) 428–438. doi:10.1098/rspa.1913.0040.

[15] R. Yuan, J. Zhang, J.-M. Zuo, Lattice strain mapping using circular hough transform for electron diffraction disk detection, Ultramicroscopy 207 (2019) 112837. doi:https://doi.org/10.1016/j.ultramic.2019.112837.

[16] R. Vincent, P. Midgley, Double conical beam-rocking system for measurement of integrated electron diffraction intensities, Ultramicroscopy 53 (3) (1994) 271 – 282. doi:10.1016/0304-3991(94)90039-6.

[17] M. P. Vigouroux, V. Delaye, N. Bernier, R. Cipro, D. Lafond, G. Audoit, T. Baron, J.-L. Rouvière, M. Martin, B. Chenevier, F. Bertin, Strain mapping at the nanoscale using precession electron diffraction in transmission electron microscope with off axis camera, Applied Physics Letters 105 (19) (2014) –. doi:10.1063/1.4901435.

[18] C. Mahr, K. Müller-Caspary, R. Ritz, M. Simson, T. Grieb, M. Schowalter, F. F. Krause, A. Lackmann, H. Soltau, A. Wittstock, A. Rosenauer, Influence of distortions of recorded diffraction patterns on strain analysis by nano-beam electron diffraction, Ultramicroscopy 196 (2019) 74 – 82. doi:https://doi.org/10.1016/j.ultramic.2018.09.010.

[19] T. C. Pekin, C. Gammer, J. Ciston, A. M. Minor, C. Ophus, Optimizing disk registration algorithms for nanobeam electron diffraction strain mapping, Ultramicroscopy 176 (2017) 170 – 176. doi:https://doi.org/10.1016/j.ultramic.2016.12.021.

[20] T. Grieb, F. F. Krause, C. Mahr, D. Zillmann, K. Müller-Caspary, M. Schowalter, A. Rosenauer, Optimization of NBED simulations for disc-detection measurements, Ultramicroscopy 181 (2017) 50 – 60. doi:https://doi.org/10.1016/j.ultramic.2017.04.015.

[21] T. Grieb, F. F. Krause, M. Schowalter, D. Zillmann, R. Sellin, K. Müller-Caspary, C. Mahr, T. Mehrtens, D. Bimberg, A. Rosenauer, Strain analysis from nano-beam electron diffraction: Influence of specimen tilt and beam convergence, Ultramicroscopy 190 (2018) 45 – 57. doi:https://doi.org/10.1016/j.ultramic.2018.03.013.

[22] G. Guzzinati, W. Ghielens, C. Mahr, A. Béché, A. Rosenauer, T. Calders, J. Verbeeck, Electron bessel beam diffraction for precise and accurate nanoscale strain mapping, Applied Physics Letters 114 (24) (2019) 243501. doi:10.1063/1.5096245.

[23] K. Müller, H. Ryll, I. Ordavo, S. Ihle, L. Strüder, K. Volz, J. Zweck, H. Soltau, A. Rosenauer, Scanning transmission electron microscopy strain measurement from millisecond frames of a direct electron charge coupled device, Applied Physics Letters 101 (21) (2012) 212110. doi:10.1063/1.4767655.

[24] K. Müller, H. Ryll, I. Ordavo, M. Schowalter, J. Zweck, H. Soltau, S. Ihle, L. Strüder, K. Volz, P. Potapov, A. Rosenauer, STEM strain analysis at sub-nanometre scale using millisecond frames from a direct electron read-out CCD camera, Journal of Physics: Conference Series 471 (2013) 012024. doi:10.1088/1742-6596/471/1/012024.

[25] K. Müller-Caspary, A. Oelsner, P. Potapov, Two-dimensional strain mapping in semiconductors by nano-beam electron diffraction employing a delay-line detector, Applied Physics Letters 107 (7). doi:http://dx.doi.org/10.1063/1.4927837.

[26] V. Özdöl, C. Gammer, M. Sarahan, A. Minor, Nano-scale Strain Mapping Using Advanced STEM with a Direct Electron Detector, Microscopy and Microanalysis 20 (S3) (2014) 1046–1047. doi:10.1017/S1431927614006953.

[27] H. Ryll, M. Simson, R. Hartmann, P. Holl, M. Huth, S. Ihle, Y. Kondo, P. Kotula, A. Liebel, K. Müller-Caspary, A. Rosenauer, R. Sagawa, J. Schmidt, H. Soltau, L. Strüder, A pnCCD-based, fast direct single electron imaging camera for TEM and STEM, Journal of Instrumentation 11 (04) (2016) P04006. doi:10.1088/1748-0221/11/04/P04006.

[28] C. Mahr, K. Müller-Caspary, M. Graf, A. Lackmann, T. Grieb, M. Schowalter, F. F. Krause, T. Mehrtens, A. Wittstock, J. Weissmüller, A. Rosenauer, Measurement of local crystal lattice strain variations in dealloyed nanoporous gold, Materials Research Letters 6 (1) (2018) 84–92. doi:10.1080/21663831.2017.1396263.

[29] J. Rouvière, Method to facilitate positioning of diffraction spots, US Patent 2013/0206968 A1 App. 13/877,904 (2013). URL http://www.google.com.ar/patents/US20130206968

[30] W. Hoppe, Beugung im inhomogenen Primärstrahlwellenfeld. I. Prinzip einer Phasenmessung von Elektronenbeugungsinterferenzen, Acta Crystallographica Section A 25 (4) (1969) 495–501. doi:10.1107/S0567739469001045.

[31] B. McCallum, J. Rodenburg, Two-dimensional demonstration of Wigner phase-retrieval microscopy in the STEM configuration, Ultramicroscopy 45 (3) (1992) 371 – 380. doi:https://doi.org/10.1016/0304-3991(92)90149-E.

[32] J. Rodenburg, B. McCallum, P. Nellist, Experimental tests on double-resolution coherent imaging via STEM, Ultramicroscopy 48 (3) (1993) 304 – 314. doi:https://doi.org/10.1016/0304-3991(93)90105-7.

[33] M. J. Humphry, B. Kraus, A. C. Hurst, A. M. Maiden, J. M. Rodenburg, Ptychographic electron microscopy using high-angle dark-field scattering for sub-nanometre resolution imaging, Nature Communications 3 (1) (2012) 730. doi:10.1038/ncomms1733.

[34] H. Yang, R. N. Rutte, L. Jones, M. Simson, R. Sagawa, H. Ryll, M. Huth, T. J. Pennycook, M. L. H. Green, H. Soltau, Y. Kondo, B. G. Davis, P. D. Nellist, Simultaneous atomic-resolution electron ptychography and Z-contrast imaging of light and heavy elements in complex nanostructures, Nature Communications 7 (2016) 12532. doi:10.1038/ncomms12532.

[35] Y. Jiang, Z. Chen, Y. Han, P. Deb, H. Gao, S. Xie, P. Purohit, M. W. Tate, J. Park, S. M. Gruner, V. Elser, D. A. Muller, Electron ptychography of 2D materials to deep sub-Angström resolution, Nature 559 (7714) (2018) 343–349. doi:https://doi.org/10.1038/s41586-018-0298-5.

[36] A. M. Maiden, J. M. Rodenburg, An improved ptychographical phase retrieval algorithm for diffractive imaging, Ultramicroscopy 109 (10) (2009) 1256 – 1262. doi:https://doi.org/10.1016/j.ultramic.2009.05.012.

[37] T. J. Pennycook, A. R. Lupini, H. Yang, M. F. Murfitt, L. Jones, P. D. Nellist, Efficient phase contrast imaging in STEM using a pixelated detector. Part 1: Experimental demonstration at atomic resolution, Ultramicroscopy 151 (2015) 160 – 167. doi:http://dx.doi.org/10.1016/j.ultramic.2014.09.013.

[38] A. Maiden, D. Johnson, P. Li, Further improvements to the ptychographical iterative engine, Optica 4 (7) (2017) 736–745.

doi:10.1364/OPTICA.4.000736.

[39] H. Yang, I. MacLaren, L. Jones, G. T. Martinez, M. Simson, M. Huth, H. Ryll, H. Soltau, R. Sagawa, Y. Kondo, C. Ophus, P. Ercius, L. Jin, A. Kovács, P. D. Nellist, Electron ptychographic phase imaging of light elements in crystalline materials using wigner distribution deconvolution, Ultramicroscopy 180 (2017) 173 – 179. doi:https://doi.org/10.1016/j.ultramic.2017.02.006.

[40] A. Rosenauer, M. Schowalter, STEMSIM - a new software tool for simulation of STEM HAADF Z-contrast imaging, in: A. Cullis, P. Midgley (Eds.), Microscopy of Semiconducting Materials 2007, Vol. 120 of Springer Proceedings in Physics, Springer Netherlands, 2008, pp. 170–172. doi:10.1007/978-1-4020-8615-1_36.

[41] F. F. Krause, M. Schowalter, T. Grieb, K. Müller-Caspary, T. Mehrtens, A. Rosenauer, Effects of instrument imperfections on quantitative scanning transmission electron microscopy, Ultramicroscopy 161 (2016) 146 – 160. doi:http://dx.doi.org/10.1016/j.ultramic.2015.10.026.

[42] F. Krause, K. Müller, D. Zillmann, J. Jansen, M. Schowalter, A. Rosenauer, Comparison of intensity and absolute contrast of simulated and experimental high-resolution transmission electron microscopy images for different multislice simulation methods, Ultramicroscopy 134 (0) (2013) 94 – 101. doi:10.1016/j.ultramic.2013.05.015.

[43] D. Cooper, J.-P. Barnes, J.-M. Hartmann, A. Béché, J.-L. Rouvière, Dark field electron holography for quantitative strain measurements with nanometer-scale spatial resolution, Applied Physics Letters 95 (5) (2009) 053501. doi:http://dx.doi.org/10.1063/1.3196549.

[44] K. Muraki, S. Fukatsu, Y. Shiraki, R. Ito, Surface segregation of In atoms during molecular beam epitaxy and its influence on the energy levels in InGaAs/GaAs quantum wells, Applied Physics Letters 61 (5) (1992) 557–559. doi:10.1063/1.107835.

[45] E. Prestat, Quantitative TEM and STEM Study of Pt-Nanoparticles Coarsening and Ge (Mn)-based Ferromagnetic Nanostructures, Ph.D. thesis, Karlsruhe, Karlsruher Institut für Technologie (KIT), Diss., 2013 (2013). doi:10.5445/IR/1000040418.

[46] A. Weickenmeier, H. Kohl, Computation of absorptive form factors for high-energy electron diffraction, Acta Crystallographica Section A 47 (5) (1991) 590–597. doi:10.1107/S0108767391004804.

[47] A. Rosenauer, M. Schowalter, J. Titantah, D. Lamoen, An emission-potential multislice approximation to simulate thermal diffuse scattering in high-resolution transmission electron microscopy, Ultramicroscopy 108 (2008) 1504–1513. doi:10.1016/j.ultramic.2008.04.002.

[48] D. Van Dyck, Is the frozen phonon model adequate to describe inelastic phonon scattering?, Ultramicroscopy 109 (6) (2009) 677 – 682. doi:DOI:10.1016/j.ultramic.2009.01.001.

[49] M. Schowalter, A. Rosenauer, J. T. Titantah, D. Lamoen, Computation and parametrization of the temperature dependence of Debye–Waller factors for group IV, III–V and II–VI semiconductors, Acta Crystallographica Section A 65 (1) (2009) 5–17. doi:10.1107/S0108767308031437.

[50] J. Rouvière, E. Sarigiannidou, Theoretical discussions on the geometrical phase analysis, Ultramicroscopy 106 (1) (2005) 1 – 17. doi:http://dx.doi.org/10.1016/j.ultramic.2005.06.001.

[51] D. Marr, E. Hildreth, S. Brenner, Theory of edge detection, Proceedings of the Royal Society of London. Series B. Biological Sciences 207 (1167) (1980) 187–217. doi:10.1098/rspb.1980.0020.

[52] A. M. Maiden, M. J. Humphry, J. M. Rodenburg, Ptychographic transmission microscopy in three dimensions using a multi-slice approach, J. Opt. Soc. Am. A 29 (8) (2012) 1606–1614. doi:10.1364/JOSAA.29.001606.

[53] P. Li, A. Maiden, Multi-slice ptychographic tomography, Scientific Reports 8 (1) (2018) 2049. doi:10.1038/s41598-018-20530-x.

[54] J. Rodenburg, A. Maiden, Ptychography, Springer International Publishing, Cham, 2019, pp. 2–2. doi:10.1007/978-3-030-00069-1_17.